




KIC 6951642: confirmed *Kepler* γ Doradus – δ Scuti star with intermediate to fast rotation in a possible single-lined binary system

A. Samadi-Ghadim¹ , P. Lampens² , and L. Gizon^{1,3,4} 

¹ Max-Planck-Institut für Sonnensystemforschung, 37077 Göttingen, Germany e-mail: samadi@mps.mpg.de

² Koninklijke Sterrenwacht van België, Ringlaan 3, B-1180 Brussel, Belgium

³ Institut für Astrophysik, Georg-August-Universität Göttingen, 37077 Göttingen, Germany

⁴ Center for Space Science, NYUAD Institute, New York University Abu Dhabi, Abu Dhabi, United Arab Emirates

September 13, 2022

ABSTRACT

Context. KIC 6951642 has been reported as a candidate hybrid pulsator of type- γ Doradus – δ Scuti from observations of the first quarters of the *Kepler* mission. The regular patterns seen in the Fourier spectra of the *Kepler* and Transiting Exoplanet Survey Satellite TESS light curves and the sinusoidal modulation of its surface brightness suggest the additional presence of rotational modulation and stellar activity, respectively.

Aims. We aim to investigate the pulsating nature of KIC 6951642 and to search for the signature of rotation and/or activity in the light curves.

Methods. We performed an iterative frequency search of both Fourier spectra, and searched for regular patterns in them. We applied spectrum synthesis to determine the atmospheric stellar parameters. Since KIC 6951642 was reported to belong to a spectroscopic binary system, we fitted the time delays derived from the light curves with the radial velocities obtained from published as well as new spectra in an attempt to improve the quality of the first orbit.

Results. Follow-up spectroscopy showed that KIC 6951642 is a fast-rotating F0-type star in a possible single-lined binary with a period of ~ 4.8 yr. In the low-frequency regime, we identified the frequencies of 0.721 d⁻¹ as well as of 0.0087 d⁻¹. We attribute the first frequency to stellar rotation, and the second one to stellar activity with a cycle of length of 3.2 yr. We also detected g modes, with the strongest mode located at 2.238 d⁻¹, as well as three asymmetric multiplets (with a mean spacing of 0.675 ± 0.044 d⁻¹). In the high-frequency regime, we detected frequencies of type- δ Scuti, with the strongest mode located at 13.96 d⁻¹, as well as seven asymmetric multiplets (with a mean spacing of 0.665 ± 0.084 d⁻¹). We subsequently identified a few more frequencies that appear to be combinations of a g or p mode and one of the higher cited frequencies not due to pulsations.

Conclusions. We propose that KIC 6951642 accommodates for a fast-rotating γ Dor – δ Sct hybrid star with various rotationally split multiplets of g and p modes and that it also displays a cycle lasting years of (possible) stellar activity.

Key words. Asteroseismology - Techniques: photometric (Fourier) - Stars: variables: δ Scuti - Stars: rotation - Stars: activity - (Stars:) binaries: spectroscopic

1. Introduction

Main-sequence A- and F-type stars are intermediate-mass stars with luminosities in the range $43 - 2 L_{\odot}$ and effective temperatures (T_{eff}) between 9800 and 6000 K (Cox 2000). As T_{eff} drops beyond ~ 7000 K and the sudden onset of convection starts (Christensen-Dalsgaard 2000; D’Antona et al. 2002), such stars are in a critical phase of transition as the regime of energy transfer in their stellar envelopes changes from (mainly) radiative to convective. This structural modification also leads to different mechanisms that can generate stellar pulsations. In this part of the H-R diagram, the pulsating stars comprise the γ Doradus (Dor), the (low- and high-amplitude) δ Scuti (Sct) stars, as well as the rapidly oscillating (magnetic) Ap stars. A detailed description of the properties of these pulsators can be found in the works by Aerts et al. (2010), Balona (2014) and Antoci et al. (2019), while a review of the recent discoveries concerning them based on the planet-searching space missions is provided by Antoci et al. (2019). Here, we provide a brief overview of the general properties of only two groups.

The mid-F- to late-A-type γ Dor stars (with masses of 1.4-1.9 M_{\odot}) pulsate in high-order, low-degree g modes with periods of

7 hr to 3 d (Kaye et al. 1999). The g modes are excited by a flux modulation mechanism at the base of the convective zone (Guzik et al. 2000; Dupret et al. 2004, 2005; Grigahcène et al. 2010).

The early-F-type to early-A-type δ Sct stars (with masses of 1.5-2.5 M_{\odot}) pulsate in low-order radial and non-radial pressure modes (p modes) with typical frequencies in the range (4 or 5) - 65 d⁻¹. These modes are mainly driven by the κ mechanism operating in the partial ionisation zone of He II (Gautschy & Saio 1995; Breger 2000), as well as by turbulent pressure which is responsible for the excitation of p modes of moderate radial order (Antoci et al. 2014; Xiong et al. 2016). Such modes allow one to probe the upper stellar layers. In unevolved δ Sct stars, most of the excited modes are p modes. However, as the star evolves and the frequency spectrum becomes denser, a large range of p modes, mixed modes (Aizenman et al. 1977; Chen & Li 2018) and g modes is predicted to be excited (Handler 2013), that is to say g modes such as those found in γ Dor stars (e.g. Balona & Dziembowski 2011).

The space missions, for example *Kepler* and Transiting Exoplanet Survey Satellite TESS (Ricker et al. 2014, 2015), revealed a new class of pulsators for which both mode-driving mechanisms operate simultaneously, that is to say the hybrid δ Sct – γ

arXiv:2209.04651v1 [astro-ph.SR] 10 Sep 2022

Table 1. Summary of previous studies concerning hybrid γ Dor– δ Scuti pulsations in binary stars.

ID	Type ^(a)	e ^(b)	Period d	$v \sin i_{1,2}$ km s ⁻¹	$M_{1,2}$ M_{\odot}	g modes d ⁻¹	p modes d ⁻¹	Act. ^(c) Cycle (d)
KIC 4544587 ⁽¹⁾	EB	0.29	2.19	86.5 75.8	1.98 1.60	γ Dor & tidal ^(d) 0.04-4.57	δ Sct 38.2-48.05	No
KIC 10080943 ⁽²⁾	EB	0.45	15.34	19.0 18.7	2.0 1.9	rot.-split ^(e) 0.6-1.45	rot.-split 12-20	No
KIC 6048106 ⁽³⁾	EB	0.01	1.56	- -	1.55 0.33	γ Dor 1.96-2.85	tid.-split ^(f) 7.49-15.2 19-22.5	Spot 290
KIC 4142768 ⁽⁴⁾	EB SB2	1.0	13.99	8.67 ^(g) 7.35 ^(g)	2.05 2.05	γ Dor & tidal 0.1-3.0	δ Sct 15-18	No
KIC 8975515 ⁽⁵⁾	SB2	0.41	1603	162 32	0.83 (q ^(h))	rot.-split 1.56-6.18	rot.-split 7.2-21.2	No
TIC 11491822 ^{(6),(i)}	EB	0.078	9.94	- -	1.94 1.51	γ Dor & tid.-split 0.11-3.51	δ Sct 5.09-18.9	No
KIC 9850387 ⁽⁷⁾	EB	0.0	2.74	13.4 -	1.66 1.06	γ Dor & tid.-split 0.11-3.51	δ Sct 10.7-16.6	No

References. (1) Hambleton et al. (2013) (2) Schmid et al. (2015) and Keen et al. (2015) (3) Samadi-Ghadim et al. (2018b) and Samadi-Ghadim et al. (2018a), Lee (2016) (4) Guo et al. (2019) (5) Samadi-Ghadim et al. (2020) (6) Southworth (2021) (7) Sekaran et al. (2020), Zhang et al. (2020) and Sekaran et al. (2021)

Notes.

^(a) Type i.e. binary classification: EB: Eclipsing Binary, SB2: double-lined Spectroscopic Binary. ^(b) e : eccentricity ^(c) Act.: any signature of stellar Activity ^(d) tidal: **tidally** excited modes ^(e) rot.-split: **rotationallysplit** modes ^(f) tid.-split: **tidallysplit** modes ^(g) $v \sin i$ from model ^(h) $q = M_2/M_1$: the mass ratio ⁽ⁱ⁾ RR Lyn

Dor stars and hybrid γ Dor– δ Sct stars. Such hybrid pulsators cover a region of the H-R diagram far more extended than the theoretical overlapping zone of the instability strips associated with each class (Balona et al. 2015; Bowman & Kurtz 2018). The simultaneous excitation of g and p modes poses a big problem from a theoretical point-of-view. There is an on-going discussion about what causes g modes in the hottest δ Sct stars (Balona & Dziembowski 2011; Balona et al. 2015; Xiong et al. 2016; Lampens et al. 2018). From asteroseismic studies of hybrid pulsators, we can infer the stellar rotation and chemical profiles from the near-to-core to the surface layers (e.g. Van Reeth et al. 2018; Li et al. 2020).

Duchêne & Kraus (2013) reported an observed frequency of spectroscopic binaries of the order of 30-45% among intermediate-mass field stars. A recent study by Moe & Di Stefano (2017) shows that the binary star fraction among A/late B stars ($M_1 = 2-5 M_{\odot}$) is $37 \pm 6\%$. Thus, we may expect a significant fraction of binaries among intermediate-mass (field) pulsators. A binary fraction of $14 \pm 2\%$ was derived by Murphy et al. (2018) from a sample of 2200 *Kepler* main-sequence A/F-type pulsators. Based on multi-epoch spectroscopy, Lampens et al. (2018) reported a multiplicity fraction of at least 27% in a sample of 49 *Kepler* hybrid pulsators of similar spectral type. As material of comparison for our study, we provide a summary of recent studies of A/F-type hybrid pulsators in binary systems in Table 1. In this table, we report some orbital and stellar parameters, the range of observed frequencies, and the origin of the frequency splittings detected among the g and p modes. Some of these pulsators in eclipsing binaries were also discussed by Lampens (2021).

In this study, we are concerned about KIC 6951642, a *Kepler* candidate for hybrid pulsations in a possible long-period binary system. We aim to decode the nature of the dominant frequencies in both the low- and high-frequency regions of its Fourier spectrum derived from *Kepler*'s full range observations. The structure of this paper is the following: Section 1 presents the general context. Section 2 describes the current status based on the literature as well as follow-up spectroscopy. We explain how we derived the atmospheric stellar properties and revised the (preliminary) orbital solution applying a combined least-squares fitting of radial velocities (RVs) and time delays (TDs). We compare the light curves available from the different surveys and describe their preparation for the study of KIC 6951642 in Sect. 3. In Sect. 4, we report our attempt concerning the search for evidence of stellar activity. We next provide the results based on the photometric (Sect. 4.1) and spectropolarimetric (Sect. 4.2) observations of KIC 6951642. Section 5 details and compares the most significant features of the Fourier spectra obtained from the *Kepler* and TESS data as well as concerning the detection of combination and harmonic frequencies in the complete frequency range. We report our results concerning the analyses of the low-frequency region and detection of the rotationally split g modes (in Sect. 6). In Sect. 7, we carefully search for δ Scuti pulsations and any signature of rotationally split p modes in the high-frequency region of the Fourier spectra. Finally, we discuss and summarise the main results of this study in Sect. 8.

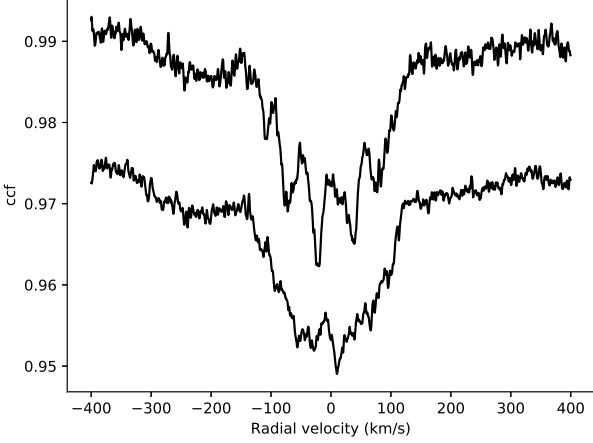


Fig. 1. CCFs from HERMES spectra collected during two different nights.

Table 2. Best-fitting set of atmospheric properties from the normalised HERMES sum spectrum of KIC 6951642.

Parameter	Value
$v \sin i$ (km s ⁻¹)	123±3
T_{eff} (K)	7336±186
$\log g$ (cgs)	3.94±0.26
[M/H] (dex)	-0.17±0.08

2. Follow-up spectroscopy

KIC 6951642 was classified as a new hybrid star in the characterisation study of the pulsational behaviour of 750 A-F-type stars observed by *Kepler* (Uytterhoeven et al. 2011). In this study based on data of Q0-Q1 (cf. their Table 3), this star presents a comparable number of low and high frequencies with the most dominant one located at 0.721 d⁻¹. It was also reported as a probable hybrid star showing both γ Dor and δ Sct oscillations by Fox-Machado & Pérez Pérez (2017). As a follow-up of the study by Uytterhoeven et al. (2011), Lampens et al. (2018) included this object among a list of 50 hybrid candidate stars to be surveyed with the high-resolution, high-efficiency spectrograph HERMES (Raskin et al. 2011). From their multi-epoch spectroscopic survey, KIC 6951642 was classified as ‘P+VAR’. Lampens et al. (2018) assigned it to class ‘P’ because the cross-correlation functions CCF display strong line-profile variations, either due to non-radial stellar pulsations (P) or to stellar rotation in the presence of surface brightness variability or spots (ROT) (Fig. 1). The plot of the radial velocities (RVs) against time (Fig. A1) indicates low-amplitude variability over a long period which is the reason for its supplementary classification ‘VAR’. Since such low-amplitude, long-term variations could also be caused by binarity, a follow-up study was necessary (cf. Sect. 2.2).

2.1. Atmospheric properties

We acquired 21 HERMES spectra of KIC 6951642 over a period of 10 years (see Table A1 for detailed information about the spectra). Based on these data, we re-derived the atmospheric stellar properties from the normalised HERMES sum spectrum. This

Table 3. Values and standard deviations of the constrained parameters of the updated orbital solution proposed for KIC 6951642.

Combined orbital solution A-B		
Parameter	Value	$\sigma^{(a)}$
P_{orb} (d)	1796	+55/-69
T_0 (HJD ^(b))	2457904	+170/-153
e	0.25	+0.14/-0.18
ω (°)	187	+36/-31
V_0 (km s ⁻¹)	-3.4	1.2
K_A (km s ⁻¹)	7.2	0.9
$a_A \sin i$ (AU)	1.14	0.12
$a_{\text{TD}} \sin i / c$ (d)	0.0066	0.0007
$f(M_B)$ (M_\odot)	0.06	0.02
rms_A (km s ⁻¹)	1.33	
rm_{TD} (d)	0.002	

Notes.

^(a) σ : Standard deviation ^(b) HJD: Heliocentric Julian Date

spectrum was evaluated against a grid of synthetic spectra to obtain the best fitting set of parameters using the tool ‘iSpec’ from Blanco-Cuaresma et al. (2014) and Blanco-Cuaresma (2019). In this comparison, we used the metal lines only. We list the corresponding set of parameters in Table 2. Figure 2 illustrates the excellent match between the observed and the synthetic spectrum in two very different wavelength ranges. The conclusion is that the spectrum of KIC 6951642 corresponds to that of a normal F0-type star. There is no trace of any additional contribution in the spectrum.

2.2. KIC 6951642 as a possible SB1: combined orbital solution

One possible mechanism to explain the slow, low-amplitude change of the RVs could be orbital motion in a binary system. Murphy et al. (2018) reported time delay variability for nine frequencies with a possible period longer than the duration of the *Kepler* data. From a simultaneous modelling of their time delays (TDs) and Lampens et al. (2018)’s RVs, they classified the target as a long-period spectroscopic binary with $P_{\text{orb}} = 1867$ d, the semi-amplitude of the light-travel time, $a_{\text{TD}} \sin i / c = 458 \pm 9$ s and the corresponding velocity semi-amplitude, $K_A = 6.1 \pm 0.2$ km s⁻¹.

We tried to improve the orbital solution of KIC 6951642 by performing a similar modelling based on the larger set of the RVs (Col. 4 of Table A1) and the TDs since the origin of the TD variability could be identical to that of the RV variability (see for example Lampens 2021).

First, we recomputed the TDs for many frequencies of the *Kepler* Fourier spectrum (Fig. 6), in particular for the dominant frequencies of the high-frequency region (where the p modes are found), but it was not possible to find a consistent behaviour for all the considered frequencies. In the next step, we selected the frequencies whose observed TDs show a long-term behaviour compatible with that of the RVs. The top panel of Fig. 3 displays the TDs of eight frequencies that show a similar general trend, whereas the bottom panel of Fig. 3 displays TDs of three other frequencies clearly showing a different trend on the long term and/or chaotic behaviour (in some parts). We re-plotted f_{43} (= 14.3778 d⁻¹) in red in the bottom panel for means of comparison

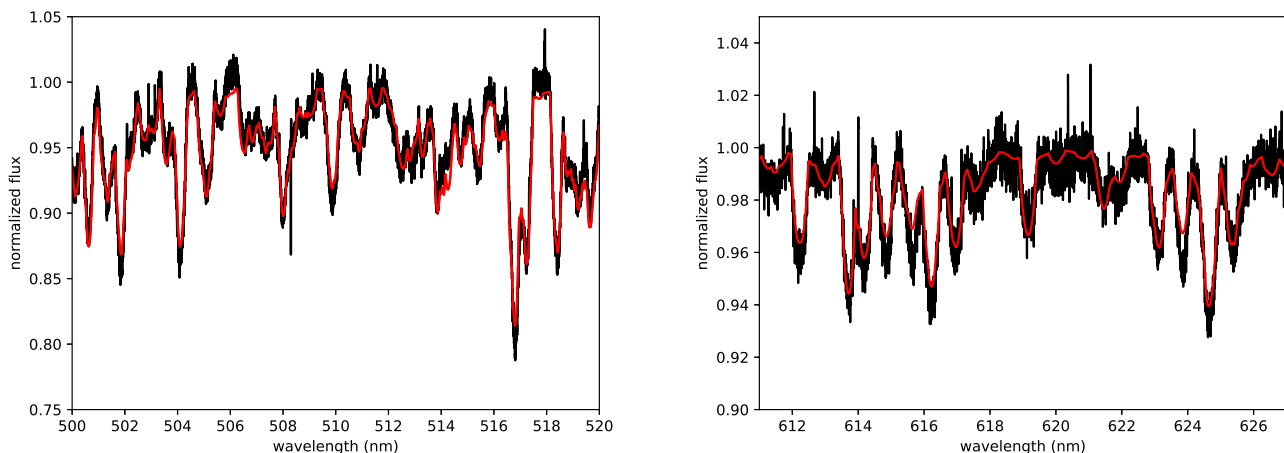


Fig. 2. Part of the HERMES sum spectrum (black) and its matching synthetic spectrum (red) *Left*: in the range 500-520 nm. *Right*: in the range 600-630 nm.

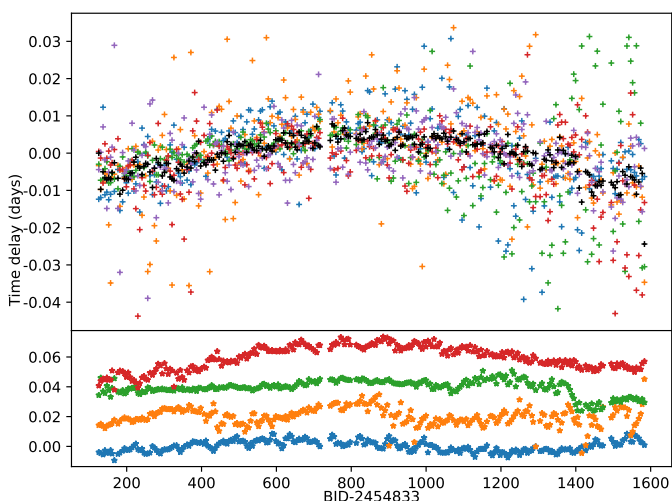


Fig. 3. TDs of high-frequencies. Top panel: eight frequencies displaying a similar long-term change: $f_{39} = 13.0064 \text{ d}^{-1}$ (f_{parent}), $f_{85} = 10.3107 \text{ d}^{-1}$ (f_{comb}), $f_{107} = 15.4706 \text{ d}^{-1}$ (f_{parent}), $f_{123} = 14.8528 \text{ d}^{-1}$ (f_{parent}), $f_{126} = 12.7318 \text{ d}^{-1}$ (f_{parent}), $f_{146} = 12.5150 \text{ d}^{-1}$ (f_{parent}), and $f_{178} = 13.7274 \text{ d}^{-1}$, $f_{43} = 14.3778 \text{ d}^{-1}$. Their mean values are plotted in black. Bottom panel: three frequencies whose behaviour is incompatible with the general trend: $f_{31} = 13.9651 \text{ d}^{-1}$ (f_{pmax} , in blue), $f_{59} = 14.9697 \text{ d}^{-1}$ (f_{parent} , in orange) and $f_{44} = 15.9634 \text{ d}^{-1}$ (f_{parent} , in green), and $f_{178} = 13.7274 \text{ d}^{-1}$, $f_{43} = 14.3778 \text{ d}^{-1}$. We re-plotted $f_{43} = 14.3778 \text{ d}^{-1}$ (f_{parent} , in red) in the lower panel for means of comparison with the frequencies that have incompatible trends in top panel. See Table 6 for the used terminology.

with the incompatible trends. By using these data together with the RVs in a simultaneous least-squares analysis, we obtained a revised solution, with the orbital parameters of Table 3. The revised orbital solution has $P_{\text{orb}} \sim 1796 \text{ d}$, $a_{\text{TD}} \sin i/c = 0.0066 \text{ d}$ (570 s) and $K_A = 7.2 \pm 0.9 \text{ km s}^{-1}$. The *rms* of the RV residuals is 1.33 km s^{-1} , that is to say larger than expected for a single-lined system (SB1) of spectral type F0, while that of the TDs is 0.002 d (Fig. 4). Due to the long period and the uncertainties, the coverage of the RV curve is far from complete. Follow-up RVs are definitely needed in the next couple of years to confirm the binary nature of KIC 6951642. The reason why some dominant pulsation frequencies fail to show a consistent long-term trend in their TDs also needs to be clarified. Some modes may

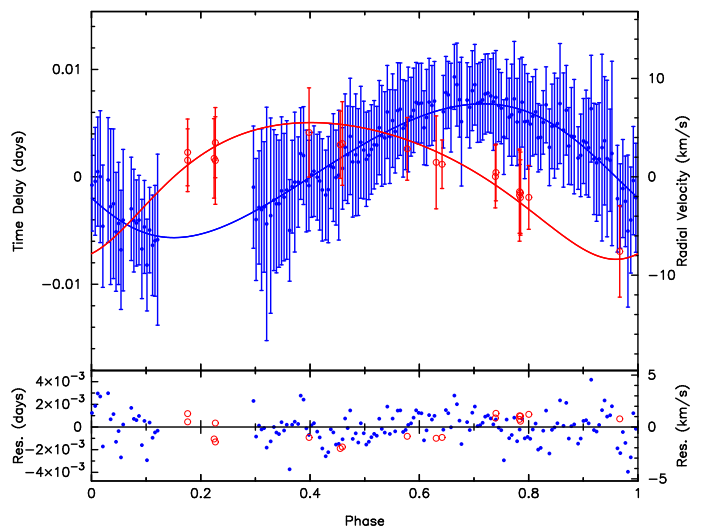


Fig. 4. Orbital solution for KIC 6951642 based on the HERMES RVs (red symbols and red solid line) and the weighted mean TD values (blue symbols and blue solid line) of eight high frequencies derived from the *Kepler* data.

present intrinsic phase changes on top of the light travel time effect (LITE). It is possible that such intrinsic variability does not allow us to find a common trend for all the p modes.

3. Available photometric data

KIC 6951642 is a bright *Kepler* object $K_p = 9.70 \text{ mag}$ (Table 4). Figure 5 shows all available light curves for KIC 6951642. We reported the information of each light curve in Table 5. The top panel in Fig. 5 illustrates the full four-year *Kepler* (1470.462 days) long-cadence (LC) observations with a sampling of 29.42 min. We normalised and stitched the light curves from different quarters with the python package 'LightKurve 2.0' (Lightkurve Collaboration et al. 2018). We removed the outliers (with $\sigma > 3$) and converted the data from flux to relative magnitude. We used the outcome of this process, the 'detrended' LC light curve, in our study. For the observed light curves in Table 5, we proceeded with the same detrending method. Figure 5 shows that the relative magnitude varies with a semi-amplitude of 8 mmag on av-

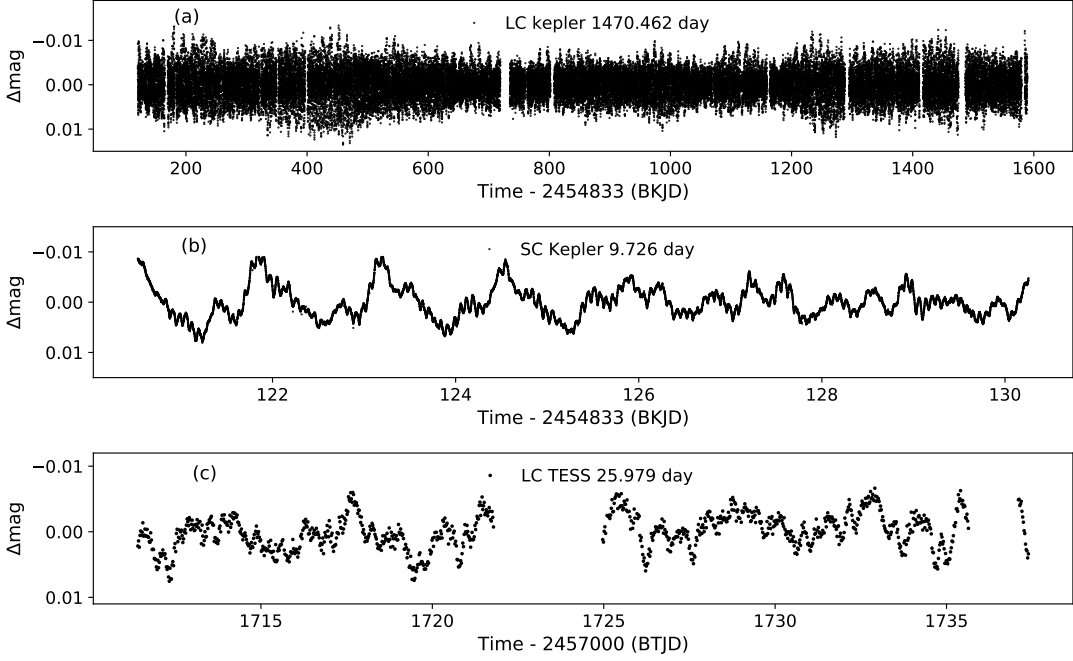


Fig. 5. Observed Light curves for KIC 6951642 from (a) *Kepler* Long Cadence (LC) (b) *Kepler* Short Cadence (SC) (c) TESS 1800-s sampling, sector 15 (Table 5).

erage in all panels. The TESS light curve (panel (c) of Fig. 5) with an 1800-s sampling rate shows the smallest semi-amplitude of all data sets (7 mmag). We can see a strong repetitive structure during the first days of the short light curve. The contamination factors reported by *Kepler* and TESS Input catalogues for KIC 6951642 are very small, that is to say 0.014 for KIC and 0.05 for TIC. We also compared the light curves derived directly from the target pixel files (TPF) for the *Kepler* and TESS data (Table 5) by applying a customised aperture mask smaller than the default aperture mask of respective pipelines (e.g. Figure 5). The light curves derived with the customised and the default masks are the same, that is to say both light curves show the same amplitudes of their variations. Hence, we conclude that the origin of the brightness variations is stellar rather than instrumental.

4. Search for evidence of stellar activity

The relative surface brightness of the LC light curve (panel (a) of Fig. 5) shows a noticeable increase at two intervals, that is to say the first ~ 500 days (Q0-Q7) and the last ~ 200 days of the observations (Q15-Q17). Indeed, KIC 6951642 shows very regularly spaced peaks in the low-frequency part of the Fourier spectrum of its *Kepler* light curve (Sect. 5), which could be indicative of the presence of a magnetic field. Hence, KIC 6951642 was a target of a spectropolarimetric survey to search for magnetic δ Scuti stars among potential candidates selected from the *Kepler* data (Thomson-Paressant et al. *in prep.*). In addition to the spectropolarimetric observations, we investigated the light curve in search of any signature of stellar activity, which we explain in this section.

4.1. Photometric observations

The stellar surface brightness may experience long-term fluctuations due to a change in the location and the size of the stellar spots (García et al. 2010). This allows us to detect the activity cycle by measuring the photospheric magnetic activity proxy S_{ph} from the light curve (Mathur et al. 2014). We derived S_{ph} using the full 4-year *Kepler* LC light curve and plotted it versus the year of the observations in Figure A2. We adopted the frequency of 0.721 d^{-1} (Uytterhoeven et al. 2011) assuming that it corresponds to the rotation frequency. Consequently, a sinusoidal behaviour of S_{ph} was observed allowing to distinguish phases of (relative) activity and inactivity. The frequency of this signal is $f_{\text{ac}} = 0.00085 \pm 0.0002 \text{ d}^{-1}$, equivalent to ~ 3.205 yr. We illustrate the best-fitting sinusoid to S_{ph} in orange in panel (b) of Fig. A2. In panel (c) of Fig. A2, we plotted the residuals emphasising their standard deviation, $\sigma = 500 \mu\text{mag}$. The frequency corresponding to S_{ph} lies very close to both the resolution frequency of the *Kepler* LC observations ($f_{\text{res}} = 0.00068 \text{ d}^{-1}$) and the (unresolved) orbital frequency ($f_{\text{orb}} = 0.00056 \pm 0.00002 \text{ d}^{-1}$).

4.2. Spectropolarimetric observations

Thomson-Paressant et al. (*private commun.*) observed KIC 6951642 with ESPaDOnS at the Canada-France-Hawaii telescope (CFHT) of the Mauna Kea Observatory in Hawaii on three different nights (April 19 and 22, and May 14, 2016). There is no sign of a magnetic field on the analysed Stokes V data with the Least-Square Deconvolution (LSD). There is no detection of any Zeeman effect in any of the three observations. The three longitudinal field values are compatible with 0 within 2σ . From the low noise level of the ESPaDOnS data, Thomson-Paressant et al. (*in prep.*) deduced that any dipolar magnetic

Table 4. Information from literature, surveys and large data bases.

Survey	Target ID
<i>Kepler</i>	KIC 6951642
TESS	TIC 63371872
Gaia	2125743657421198592
KIC ^(a)	
RA	19 ^h 31 ^m 05.93 ^s
Dec	+42°29′53.20″
Kp (mag)	9.70
T _{eff} (K)	7178
log <i>g</i> (cgs)	3.365
R (R _⊙)	4.413
Gaia DR2 ⁽¹⁾	
ϖ (mas)	1.7272±0.0257
distance ⁽²⁾ (pc)	569.6085
m _G (mag)	9.60
Gaia DR3 ⁽³⁾	
ϖ (mas)	1.7077±0.0153
m _G (mag)	9.61

References. (1) Gaia Collaboration et al. (2016), Gaia Collaboration et al. (2018a) and Gaia Collaboration et al. (2018b) (2) Bailer-Jones et al. (2018)(3) Lindegren et al. (2021), Gaia Collaboration et al. (2021) and Halbwachs et al. (2022)

Notes.

^(a) from the *Kepler* Input Catalogue (based on 5-band photometry, plus the J, H, & K bands from the 2MASS survey, assuming that the object is a single star.)

Table 5. Available photometric data for KIC 6951642.

Parameter/Survey	<i>Kepler</i> LC	<i>Kepler</i> SC	TESS ^(b)
T (d)	1470.462	9.726	25.979
Δt (min)	29.424	0.981	29.999
T _{ref} (BJD)	2454833	2454833	2457000
f_{res} (d ⁻¹)	0.00068	0.10282	0.03849
f_{Nyq} (d ⁻¹)	24.469	734.074	24.001
interval	Q0-Q17	Q0	S15
year	2009-2013	2009	2019

Notes. T: Time span of the observations. Δt : mean time sampling of the observations. f_{res} : Resolution frequency. f_{Nyq} : Nyquist frequency.

^(b) pipeline: TESS Light Curves From Full Frame Images (TESS-SPOC)

field B >~300 G at the pole is detectable in the ESPaDOnS data with a probability of 90%.

5. Fourier analysis and combination frequencies

Our approach for Fourier analysis is the Lomb-Scargle periodogram (Lomb 1976; Scargle 1982). To determine the significant frequencies, we applied prewhitening. That is to say a sinusoid with the frequency of that highest peak in the periodogram is fitted to the light curve and subsequently subtracted from the light curve, iteratively. We calculated the Fourier spectrum of all three data sets (Table 5 & Fig. 5) up to twice their Nyquist frequency, f_{Nyq} in Table 5. The signal-to-noise ratio

(S/N) of the frequencies is the mean of the periodogram over a window size of 1 d⁻¹. We adopted the much used criterion S/N ≥ 4 (Breger et al. 1993) to consider a frequency as significant in this study. We consider that two frequencies are well resolved if their difference agrees with $f_i - f_j \geq 1.5/T$, with T the time span of the observation. f_{res} (or 1/T) for the *Kepler* LC observations equals 0.00068 d⁻¹ (see Table 5 for the other observations). From each pair of frequencies that did not fulfil this criterion, we ignored the frequency of smaller amplitude. We obtained a list of 593 well-resolved frequencies from this procedure, called ‘significant frequencies’ hereafter.

Figure 6 shows the original Fourier spectra of the *Kepler* LC (panel a), *Kepler* SC (panel b) and TESS light curves (panel c). For the *Kepler* LC and TESS spectra, we indicate the limiting Nyquist frequency with a vertical red line. We plotted a closer view of the Fourier spectrum of the *Kepler* SC light curve in the range of the Nyquist frequency (panel (b) in Fig. 6) to compare with the *Kepler* LC spectrum. The larger frequency range in SC spectrum, that is to say 48-734 d⁻¹, doesn’t include any significant frequency, so we cut that frequency region in panel (b) Fig. 6. It is clear from the three spectra that there are two frequency ranges below the Nyquist regime where the frequencies with the largest amplitudes appear, that is to say at 0.2-4.0 d⁻¹ and 10-17 d⁻¹ intervals. In the super-Nyquist regime, the (still well resolved) mirrored frequencies appear with amplitudes either smaller than (*Kepler*) or equal to (TESS) those of the already detected frequencies. To study the pulsations, we used the *Kepler* LC Fourier spectrum.

A close look to the low- and high-frequency regions of the three Fourier spectra (Fig. A3) confirms the presence of the most dominant frequencies in all of them. However, the amplitudes of the corresponding frequencies vary quite significantly from spectrum to spectrum.

The forest of frequencies found in hybrid (δ Sct– γ Dor or γ Dor– δ Sct) stars can include frequencies that are actually a linear combination of several independent frequencies with the highest S/N and largest amplitudes, named ‘parent frequencies’ hereafter. We marked the adopted parent frequencies as ‘ f_{parent} ’ (in magenta) in Tables A2 (low-frequency region) and A3 (high-frequency region). We carefully considered all remaining frequencies of both the low- and high-frequency regions in our search for linear combinations of the parent frequencies. We consider that a frequency is a combination (resp. a harmonic) frequency if the difference between the calculated combination (resp. harmonic) frequency and the candidate frequency is smaller than f_{res} (e.g. Zhang et al. 2018). The third most dominant frequency in the Fourier spectrum is f_3 (= 0.721 d⁻¹) with an amplitude A_3 equal to 1.1 mmag. The uncertainties on all the significant frequencies are as large as $\epsilon_f = (0.04 - 3) \times 10^{-4}$ d⁻¹. We remark that it is the dominant one in the *Kepler* SC periodogram (see also Uytterhoeven et al. 2011). Since we also identified the first and second harmonics of f_3 , namely f_{34} (= 1.442 d⁻¹) and f_{215} (= 2.163 d⁻¹), we consider that f_3 is a good candidate for the rotational frequency f_{rot} of the fast-rotating star in the system. Among the frequencies detected in both regions of the Fourier spectrum, we recognised the following three combination types:

- (i) $f_i = n f_{\text{parent}_i} \pm m f_{\text{parent}_j}$ ($n, m = 1, 2, 3$):

That is to say linear combinations of the parent frequencies. Such frequencies are marked in blue on panels (a) of Fig. 7 (for the low-frequency region: $f < 5.0$ d⁻¹) and Fig. 9 (for the high-frequency region: $f \geq 5.0$ d⁻¹).

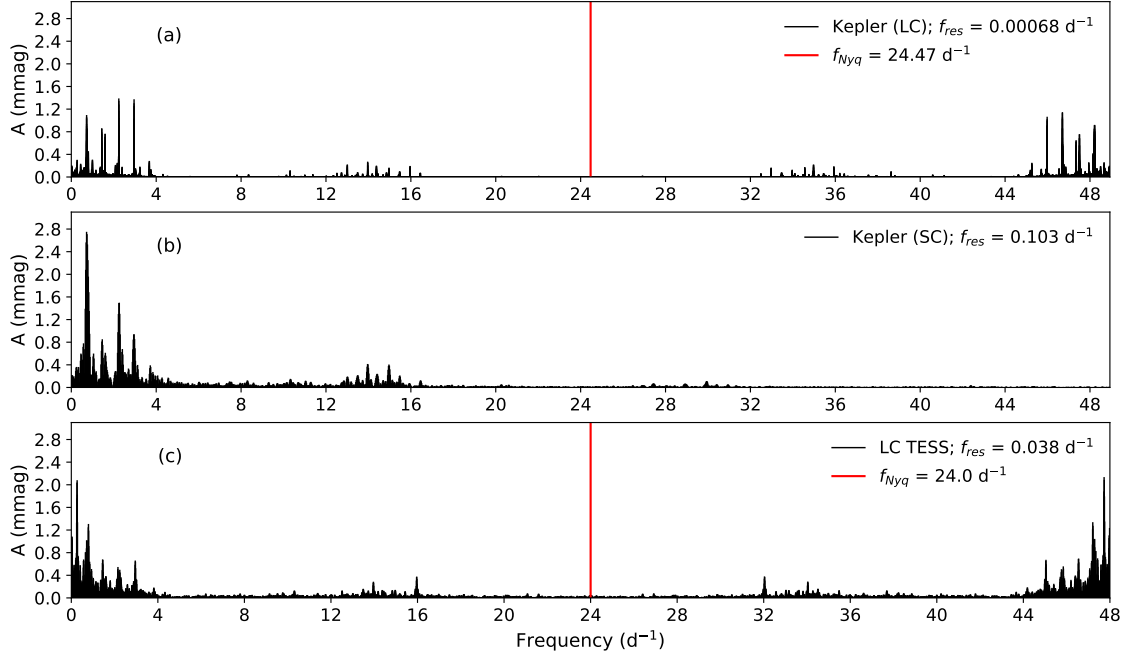


Fig. 6. Fourier Spectra for KIC 6951642 from (a) *Kepler* Long Cadence (LC) (b) *Kepler* Short Cadence (SC) (c) TESS 1800-sec, sector 15. The spectra in (a) and (c) are calculated up to their double Nyquist frequencies.

Table 6. Terminology used to describe the combination frequencies found in the Fourier spectrum of KIC 6951642 (Sect. 5).

Frequency	Description	value (d^{-1})	Colour
f_{ac}	the frequency of long-term stellar activity	0.00085 ± 0.0002	–
f_{ach1}	$f_{117} \sim 9^{\text{th}}$ harmonic of f_{ac}	0.0087	green
f_{ach2}	$f_{169} \sim 9^{\text{th}}$ harmonic of f_{ach1}	0.0856	green
f_{rot}	f_3 , the candidate rotational frequency	0.721	red
f_{parent}	the parent g and p modes		magenta
f_{pmax}	f_{31} , the highest amplitude p mode	13.965	violet

Notes. The uncertainties in frequency are of the order of $\epsilon_f = (0.04 - 3) \times 10^{-4} \text{ d}^{-1}$. Col. ‘Colour’ refers to the colors in Tables A2 and A3.

The relevant information for the detected combinations is mentioned under the columns ‘combs’ and ‘remark’ in Tables A2 and A3. An explanation of the used terminology is provided in Table 6.

(ii) $f_i = n f_{\text{parent}} \pm m f_{\text{rot}}$ ($n, m = 1, 2, 3$):

That is to say combinations of the parent frequencies (or their harmonics) and f_{rot} (or its harmonics). Such frequencies are marked in orange across the entire Fourier spectrum on panel (a) of Figs. 7 and 9 (resp. $f < 5.0 \text{ d}^{-1}$ and $f \geq 5.0 \text{ d}^{-1}$). We marked f_{rot} and its harmonics with red pluses on panel (b) of Fig. 7. These combinations are also listed in Tables A2 and A3.

(iii) $f_i = n f_{\text{parent}} \pm m f_{\text{ach}_{1,2}}$ ($n, m = 1, 2, 3$):

We furthermore detected two probable high-order harmonics of f_{ach} (see Section 4.1) in the Fourier spectrum: the first one ($f_{117} = 0.0087 \text{ d}^{-1}$) is called f_{ach1} and the second one ($f_{169} = 0.0856 \text{ d}^{-1}$) is called f_{ach2} in Table 6. These frequencies are marked in green in Tables A2 and A3 as well as in panel (a) of Fig. 7. We detected a couple of com-

binations of the parent frequencies and both of these frequencies.

6. The low-frequency region and rotational splitting of g modes

Panel (a) of Fig. 7 presents a closer view of the low-frequency region of the object’s Fourier spectrum ($f < 5.0 \text{ d}^{-1}$). We derived 309 frequencies with $\text{S/N} \geq 4.0$. We list 97 of them with amplitudes larger than 0.08 mmag in Table A2. Column f_i of Table A2 shows the frequencies sorted in descending order of amplitude. The mean amplitude and mean S/N are $A_{\text{mean}} = 0.121 \text{ mmag}$ and $\text{S/N}_{\text{mean}} = 8.4$. The highest-amplitude frequency occurs at $f_1 = 2.238 \pm 4 \times 10^{-5} \text{ d}^{-1}$ (with $A_1 = 1.3910 \pm 0.0015 \text{ mmag}$ and $\text{S/N} = 59$).

Many γ Dor/ δ Sct stars experience intermediate to fast rotation. Hence, the first-order approximation in the traditional approximation of stellar rotation (TAR) does not hold anymore (e.g. Reese et al. 2008; Bouabid et al. 2013). In this case, the frequency spacing is no longer a constant. When higher-order rotation terms become significant, we no longer expect symmetric

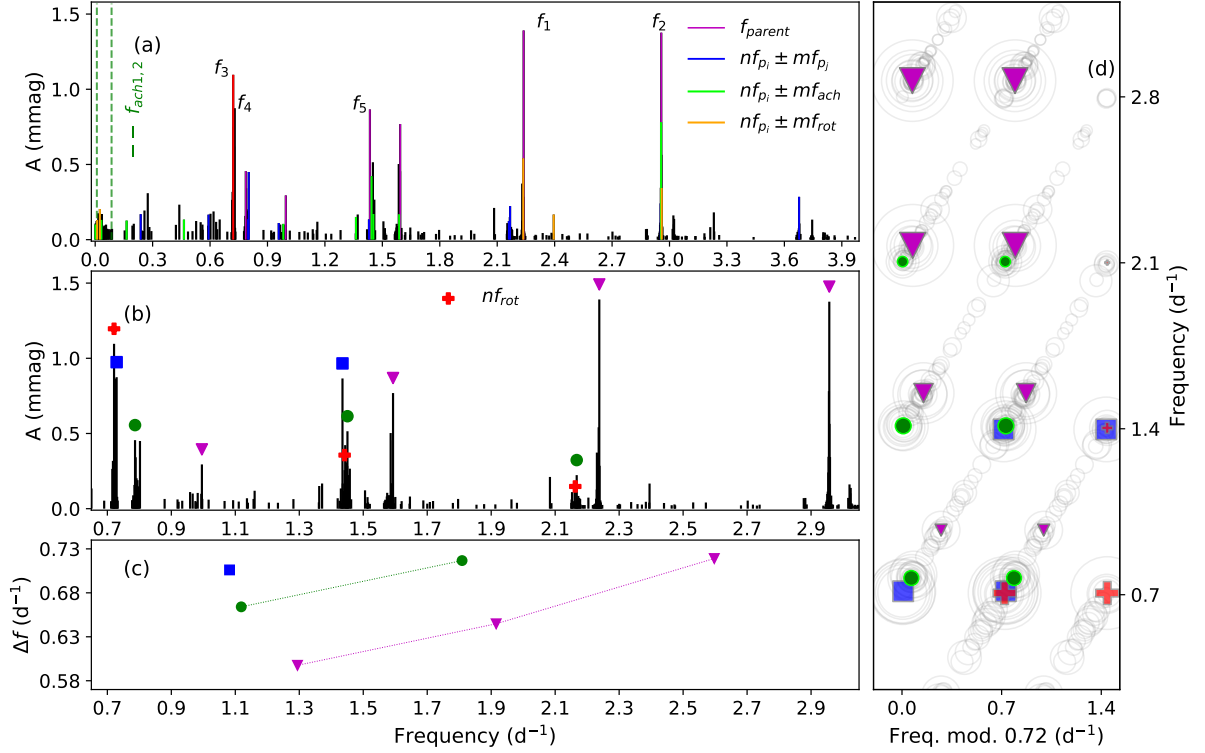


Fig. 7. Low-frequency region ($f \leq 5 \text{ d}^{-1}$) of the Fourier spectrum for the full *Kepler* LC observations of KIC 6951642. (a) Different types of combination frequencies are detected among the significant frequencies of this region (Table A2). For the terminology, see Table 6. f_{1-5} represent the frequencies in descending order of amplitude (Table A2.) (b) Identification of the rotational frequency: the frequencies shown with red pluses show the rotational frequency and its first and second harmonics (Table 7). (c) Detection of rotationally split values for the multiplets in panel (b) (Table 7). (d) The échelle diagram for the multiplets in panel (b). Grey circles represent the significant low frequencies. The marker's size is linked to the amplitude of the frequency. Colours and indicators follow the descriptions of panels (b) & (c).

Table 7. Multiplets of asymmetrically split g modes.

f_i	f d^{-1}	A mmag	S/N	$\Delta f \pm \sigma_{\Delta f}$ d^{-1}	marker
f_{16}	0.7866	0.4557	17		●
f_{13}	1.4506	0.5148	22	0.664 ± 0.004	●
f_{38}	2.1673	0.2231	16	0.717 ± 0.016	●
f_{27}	0.9956	0.2943	13		▲
f_8	1.5932	0.7688	29	0.598 ± 0.029	▲
f_1	2.2380	1.3910	59	0.645 ± 0.011	▲
f_2	2.9570	1.3764	77	0.719 ± 0.017	▲
f_4	0.7290	0.8743	27		■
f_5	1.4351	0.8659	30	0.706 ± 0.012	■

Notes. The mean spacing is $\Delta f_{\text{mean}} = 0.675 \pm 0.044 \text{ d}^{-1}$. The error is the standard deviation associated with the mean spacing. The column 'marker' shows the symbols and colours for each multiplet of Fig. 7.

multiplets (Saio 1981). Some examples are mentioned in Table 1. Our estimation of M_V , based on distance derived for all Gaia DR2 targets by Bailer-Jones et al. (2018) (Table 4), is ~ 0.92 mag for the entire system (ignoring the extinction as the star is located at ~ 570 pc). By assuming a magnitude difference of at least 1.5 mag for the companion (Batten 1973), we find $M_V = 1.19$ mag for the pulsating component. Accordingly, we derived

$\log L/L_\odot \approx 1.41$ from M_V . Using $T_{\text{eff}} = 7336 \text{ K}$ from Table 2, we derive an average radius of $3.15 R_\odot$. From the mass-luminosity relation $L = L_\odot (M/M_\odot)^{3.9}$ (Cox 2000), we estimate a mass of approximately $2.3 M_\odot$ for the primary. Considering the critical Keplerian angular velocity Ω_K as $\Omega \ll \Omega_K \equiv \sqrt{GM/R^3}$; with G the universal constant of gravity, M the stellar mass and R the derived mean stellar radius and f_3 as the rotation frequency, we obtain $\Omega/\Omega_K = 75\%$ for the fast-rotating companion. Using the polar radius to derive Ω ($R_{\text{equatorial}} = 3/2 R_{\text{mean}}$) results in an even larger Ω/Ω_K ratio. Hence, we may expect to find multiplets that are affected by asymmetric splitting.

The second highest-amplitude frequency, $f_2 = 2.957 \pm 4 \times 10^{-5} \text{ d}^{-1}$, has an amplitude very similar to f_1 , $A_2 = 1.3764 \pm 0.0016$ mmag and S/N = 77. We suggest that f_1 and f_2 are the members of a multiplet with Δf values increasing from $0.598 \pm 0.029 \text{ d}^{-1}$ to $0.719 \pm 0.017 \text{ d}^{-1}$ (which lies close to f_3). We marked this multiplet with magenta triangles in panel (b) of Fig. 7. f_{rot} (Table 6 & Sect. 5) and its harmonics are labelled with red plus marks. Panel (b) is a closer view of the region between 0.7 and 3.0 d^{-1} . In this region, we detected two other series of retrograde g modes with a minimum spacing value of $\Delta f = 0.664 \pm 0.004 \text{ d}^{-1}$ and a maximum spacing value of $\Delta f = 0.717 \pm 0.016 \text{ d}^{-1}$ (which lies close to f_3). The quoted errors represent the standard deviation associated with the mean value of all three multiplets, that is to say $\Delta f \pm \sigma_{\Delta f} = 0.675 \pm 0.044 \text{ d}^{-1}$. Panel (c) of Fig. 7 shows the Δf values for the different g modes, with their associated marker and colour in panel (b) and Table 7. We suggest that the detected

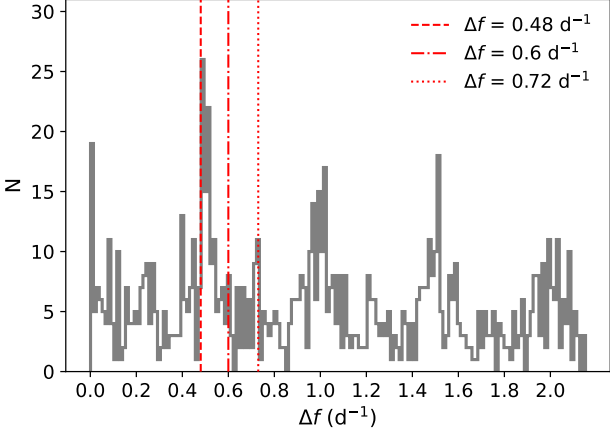


Fig. 8. Histogram of all possible frequency spacings for the parent p modes between 7.0–17.0 d^{-1} (Table A3). Three highest peaks, excluding the harmonics of 0.48, are indicated with red lines.

multiplets are due to intermediate or fast rotation, which causes them to be split asymmetrically. We marked these frequencies with the label 'RS' (Rotationally Split) in the column 'remark' of Table A2. In panel (d) of Fig. 7, we plotted all the frequencies in an échelle diagram using the frequency modulo the (candidate) rotation frequency $f_{\text{rot}} = 0.721 \text{ d}^{-1}$ on the X-axis. We see that the multiplets are arranged on wiggled vertical ridges, indicative of modes with the same degree ℓ . However, we couldn't identify any period spacing pattern among g modes (according to asymptotic relation for g modes.)

7. The high-frequency region and rotational splitting of p modes

Panel (a) of Fig. 9 presents a closer view of the high-frequency region of the Fourier spectrum ($f \geq 5.0 \text{ d}^{-1}$). We derived 284 frequencies with $\text{S/N} \geq 4.0$. We list 55 of them with amplitudes larger than 0.019 mmag in Table A3. Column f_i of Table A3 shows the frequencies sorted in descending order of amplitude. The mean amplitude and mean S/N are $A_{\text{mean}} = 0.0193 \text{ mmag}$ and $\text{S/N}_{\text{mean}} = 7.72$. The highest-amplitude frequency occurs at $f_{31} = 13.9651 \pm 2 \times 10^{-5} \text{ d}^{-1}$ (with $A_{31} = 0.2718 \pm 0.008 \text{ mmag}$ and $\text{S/N} = 54$).

In the search for regular patterns, we calculated all possible frequency spacings between all the pairs of parent frequencies (p modes). These parent frequencies are labelled as f_{parent} in magenta under the column 'remark' in Table A3 (Sect. 5). We illustrate the distribution of the spacings in Fig. 8. The most frequent spacing values are located at $\sim 0.48 \text{ d}^{-1}$ and its harmonics. Excluding the mentioned most frequent spacings the other two peaks are located at 0.6 d^{-1} , and 0.72 d^{-1} . We recall that 0.721 d^{-1} equals the rotation frequency as discussed in Sect. 5. The first detection represents a quintuplet of rotationally split p modes centred around f_{31} , with mean frequency spacing $\Delta f = 0.727 \pm 0.005 \text{ d}^{-1}$ (equivalent to f_{rot}). In panel (b) of Fig. 9, we marked the frequencies of this multiplet with green triangles. The same figure illustrates six more rotationally split multiplets of retrograde and prograde p modes. Panel (c) of Fig. 9 displays the Δf values of these multiplets. We list these values in Table 8. The uncertainty in the frequency spacing, $\sigma_{\Delta f}$, represents the standard deviation of the mean value. The detected splittings are asymmetric on both sides. Their values range from $0.483 \pm 0.065 \text{ d}^{-1}$ to $0.729 \pm 0.028 \text{ d}^{-1}$ (similar to f_3). The mean spacing for all

Table 8. Multiplets of asymmetrically split p modes.

f_i	f d^{-1}	A mmag	S/N	$\Delta f \pm \sigma_{\Delta f}$ d^{-1}	marker
f_{434}	10.4774	0.0108	4		X
f_{230}	11.0008	0.0436	15	0.523 ± 0.050	X
f_{463}	11.7093	0.0098	4	0.708 ± 0.020	X
f_{328}	10.8299	0.0218	8		■
f_{210}	11.3772	0.0497	18	0.547 ± 0.041	■
f_{331}	12.0166	0.0213	8	0.639 ± 0.006	■
f_{126}	12.7318	0.0823	24	0.715 ± 0.023	■
f_{223}	13.4492	0.0450	15	0.717 ± 0.023	■
f_{288}	12.3408	0.0281	11		●
f_{39}	13.0064	0.2219	53	0.666 ± 0.004	●
f_{178}	13.7274	0.0606	18	0.721 ± 0.025	●
f_{154}	14.4500	0.0689	20	0.723 ± 0.025	●
f_{146}	12.5150	0.0708	22		▲
f_{260}	13.2328	0.0341	12	0.718 ± 0.024	▲
f_{31}	13.9651	0.2718	54	0.732 ± 0.029	▲
f_{213}	14.6942	0.0485	16	0.729 ± 0.028	▲
f_{226}	15.4231	0.0441	16	0.729 ± 0.028	▲
f_{43}	14.3778	0.2018	43		*
f_{59}	14.9697	0.1652	39	0.592 ± 0.024	*
f_{259}	14.1668	0.0341	12		◆
f_{123}	14.8528	0.0841	23	0.686 ± 0.012	◆
f_{107}	15.4706	0.0976	28	0.618 ± 0.014	◆
f_{44}	15.9634	0.1948	53	0.493 ± 0.061	◆
f_{453}	15.2490	0.0102	5		+
f_{104}	15.9627	0.0985	30	0.714 ± 0.022	+
f_{135}	16.4458	0.0766	27	0.483 ± 0.065	+

Notes. The mean spacing is $\Delta f_{\text{mean}} = 0.665 \pm 0.084 \text{ d}^{-1}$. The error value is the standard deviation associated with the mean spacing. The column 'marker' shows the symbols and the colours of each multiplet in Fig. 9.

seven multiplets is $\Delta f_{\text{mean}} = 0.665 \pm 0.084 \text{ d}^{-1}$. We suggest that all detected multiplets are due to intermediate or fast rotation, which causes them to be split asymmetrically. Thus, we observe the same behaviour as with the multiplets of the g modes. In Table 8, we list the frequency, the amplitude and the S/N of each multiplet. We indicate these frequencies with the label 'RS' (Rotationally Split) in the column 'remark' of Table A2.

In panel (d) of Fig. 9, we plotted all the frequencies between 10–17 d^{-1} in an échelle diagram using the frequency modulo the rotation frequency $f_{\text{rot}} = 0.721 \text{ d}^{-1}$ on the X-axis. We present the frequencies with grey circles with their sizes associated with their amplitudes. The frequencies whose TDs show a similar long-term trend (annotated as 'TDR' in Table A3 and in the upper panel of Fig. 3) are presented with black circles in Fig. 9, six ($f_{39, 107, 123, 126, 146, 178}$) of which belong to rotationally split multiplets. The frequencies showing incompatibility with the general trend ('TDir' in Table A3 and in the bottom panel of Fig. 3) are represented by brown circles, three ($f_{31, 43, 44}$) of which belong to multiplets ($f_{31} \equiv f_{p_{\text{max}}}$).

The pulsation constants (Breger 1990) Q of the parent (shown as black circles in Fig. 10) and the rotationally split p modes (shown as red circles in Fig. 10) were derived using T_{eff} and $\log g$ from Sect. 2.2 as well as M_{bol} based on the Gaia DR3 parallax (Lindgren et al. 2021) (see Table 4).

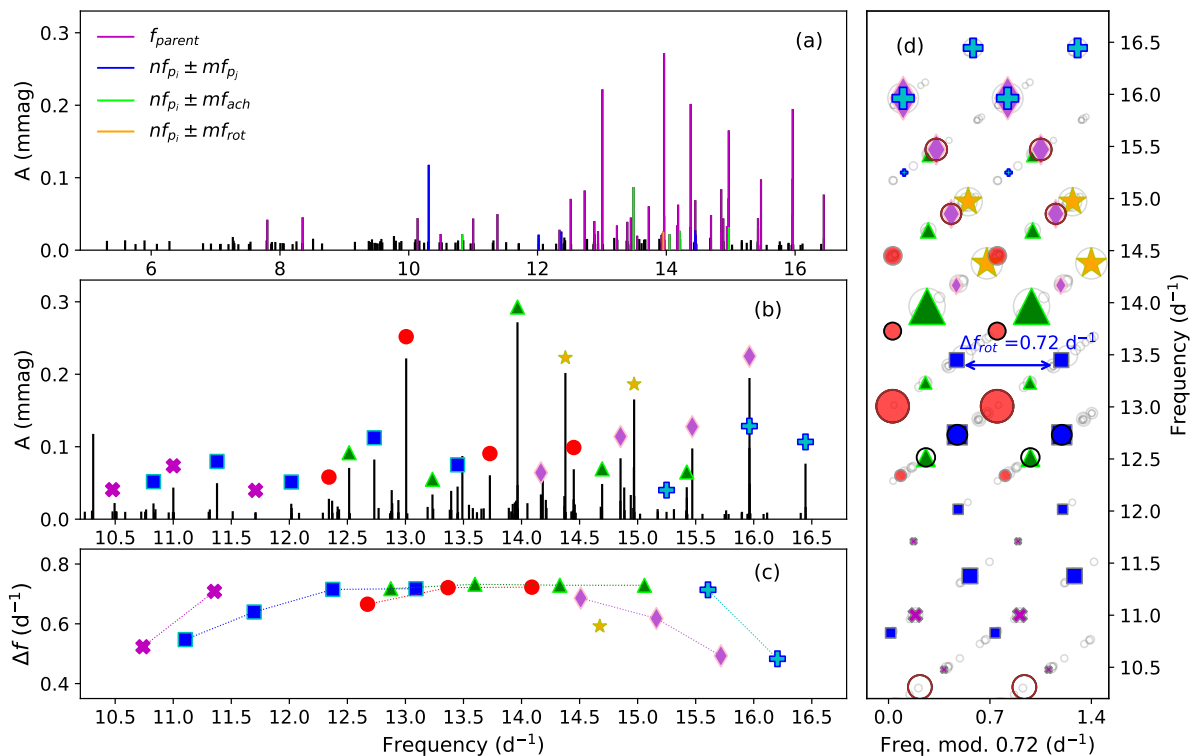


Fig. 9. High-frequency region ($f \geq 5 \text{ d}^{-1}$) of the Fourier spectrum for the full *Kepler* LC observations of KIC 6951642. (a) Different types of combinations are detected among the significant frequencies ($S/N \geq 4$) (Table A3). (b) Detection of rotationally split p modes in the interval $(10.5-17) \text{ d}^{-1}$ ($\Delta f_{\text{rot}} \equiv f_3 = 0.721 \text{ d}^{-1}$) (Table 8). (c) Detection of rotationally split values for the multiplets in panel (b) (Table 8). (d) The échelle diagram for the detected multiplets in panel (b). Grey circles: the significant high-frequencies. The marker's size is linked to the amplitude of the significant frequency. Black circles: The frequencies whose TDs show a similar long-term time delay trend (TDr in Table A3). Brown circles: The frequencies showing incompatibility with general long-term time delay trend (TDir in Table A3). Colours and indicators follow the descriptions of panels (b) & (c).

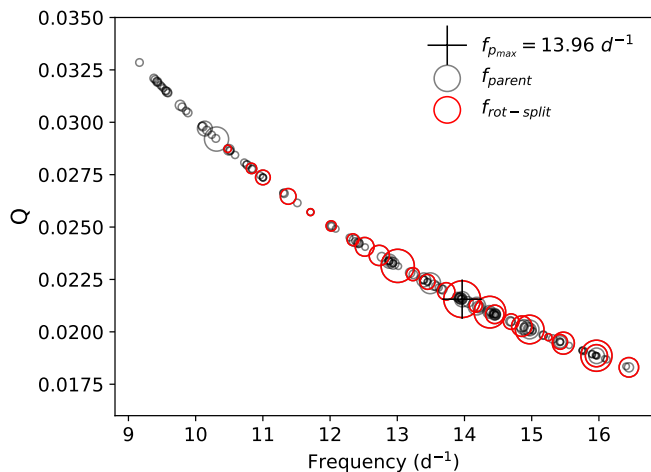


Fig. 10. Pulsation constants Q for the high frequencies revealed by the Fourier spectrum of KIC 6951642. Black circles show the parent frequencies (see Table A3). Red circles show the rotationally split p modes (see Table 8). The marker's size is associated with the amplitude of the p modes.

8. Discussion and conclusions

KIC 6951642 is a *Kepler* object of magnitude $K_p = 9.70$ mag. It was introduced as a candidate hybrid γ Dor– δ Sct star from studies of the *Kepler* light curves by Uytterhoeven et al. (2011), who reported the highest-amplitude mode of 0.721 d^{-1} , and by Fox-Machado & Pérez Pérez (2017). The low-amplitude variability in the RVs collected from multi-epoch spectroscopy with HERMES (Lampens et al. 2018) as well as the study of the TDs of nine high frequencies (Murphy et al. 2018) suggest that KIC 6951642 is a (single-lined) binary system. Spectroscopic analysis shows that it is a normal F0-type star with $T_{\text{eff}} = 7336 \pm 186 \text{ K}$. The combination of the RV curve with the TDs of eight significant high frequencies detected in the *Kepler* LC Fourier spectrum lead to an updated orbit with P_{orb} almost equal to 1800 d. Due to the incompleteness of the data (e.g. RV data are lacking in the phase intervals 0-0.2 and 0.8-0.95, cf. Fig. 4) and the lack of consistent behaviour in the TDs, the confirmation of its binary nature is not (yet) feasible and more spectroscopic observations will be needed. Currently, we consider it as a *possible* binary system.

Although the spectropolarimetric observations of KIC 6951642 do not show any Zeeman signature as evidence of a magnetic field, we detected a sinusoidal behaviour with a period of ~ 3.2 yr from analysis of S_{ph} in the *Kepler* LC light curve ($f_{\text{ac}} = 0.00085 \pm 0.0002 \text{ d}^{-1}$). Accordingly, at the first date of the spectropolarimetric observations (Apr. 19, 2019) the star was in a

state of minimum activity (in the 1.96th year of the *Kepler* mission, see panel (b) of Fig. A2). This could be the reason for the unsuccessful detection of magnetic activity from the spectropolarimetric observations. The same argument explains why the TESS light curve has a lower amplitude compared to the *Kepler* LC light curve. The first date of the TESS observations (Aug. 15, 2019) occurred during a state of minimum activity (in the 2.29th year of the *Kepler* mission, see panel (b) of Fig. A2). Unfortunately, since the cycle length is similar to the time span of the observations, we do not know what causes the suggested activity.

The atmospheric stellar parameters locate KIC 6951642 in the overlapping area of the δ Sct– γ Dor instability strips. We used the relation $R \sin i = v \sin i \cdot P_{\text{rot}} / 50.58$ to infer a lower limit for the stellar radius, with v the equatorial velocity, $v \sin i$ the projected rotational velocity (km s^{-1}), and P_{rot} the estimated rotation period (d). This gives a minimum radius of $3.4 R_{\odot}$, that is to say too large for a normal F0-type star. On the other hand, the study of δ Sct stars in eclipsing binaries (García Hernández et al. 2017) demonstrates that somewhat evolved δ Sct stars have radii larger than normal. The radius derived from the Gaia DR2 distance (Table 4 Bailer-Jones et al. 2018), and T_{eff} (cf. Table 2) equals $3.15 R_{\odot}$, almost the value derived by assuming $f_3 = f_{\text{rot}}$. Hence, this confirms that the fast-rotating object in KIC 6951642 is an evolved F0-type star.

From the Fourier spectrum of the *Kepler* LC light curve, 593 significant frequencies with $S/N \geq 4$ were extracted. The spectrum also reveals a strong regularity in both the low- and high-frequency regions. In the high-frequency region, we detected several p modes in the range of $10\text{--}17 \text{ d}^{-1}$. The p mode of highest amplitude is $f_{p_{\text{max}}} = 13.965 \text{ d}^{-1}$ ($A_{p_{\text{max}}} = 0.27 \text{ mmag}$). We detected seven rotationally split multiplets comprising 26 p modes with $\Delta f_{\text{mean}} = 0.665 \pm 0.084 \text{ d}^{-1}$.

In the low-frequency region, we identified $f_3 = 0.721 \text{ d}^{-1}$ and its first and second harmonics. We detected two frequencies close to high harmonics of f_{ac} , a probable signature of stellar activity, in the Fourier spectrum (f_{ach1}) $f_{177} = 0.0085 \text{ d}^{-1}$ and $f_{169} = 0.0856 \text{ d}^{-1}$ (f_{ach2}). We also detected several frequencies that are linear combinations of one of these three frequencies (f_{rot} , f_{ach1} and f_{ach2}) or their second and third harmonics with either a g or a p mode. We cannot explain the occurrence of such high harmonics of f_{ac} (i.e. $10f_{\text{ac}}$ and $100f_{\text{ac}}$). We identified the two most dominant frequencies in the Fourier spectrum ($f_1 = 2.238 \text{ d}^{-1}$ and $f_2 = 2.957 \text{ d}^{-1}$, $A_{1,2} \approx 1.4 \text{ mmag}$) as members of a retrograde multiplet split by rotation. We detected two other multiplets of rotationally split g modes. The mean frequency spacing for the three multiplets of g modes equals $\Delta f_{\text{mean}} = 0.675 \pm 0.044 \text{ d}^{-1}$. Accordingly, we associate the multiplets of g and p modes to the fast-rotating (component of) KIC 6951642 ($\Omega/\Omega_K = 75\%$), suggesting that f_3 is the rotational frequency. From the detected Δf_{mean} for both g and p modes, we derive a ratio of 1.02 ± 0.14 for the core-to-surface rotation, that is to say compatible with solid-body rotation. We couldn't identify any sensible period-spacing pattern matching the usual properties of γ Dor pulsations.

In summary, this study confirms the occurrence of γ Dor pulsation modes covering an extended range from 0.72 to 2.4 d^{-1} due to significant stellar rotation and δ Sct pulsation modes covering the frequency range $10\text{--}17 \text{ d}^{-1}$ for the fast-rotating and (probably) active (companion) star KIC 6951642. Hence, we confirm the genuine hybrid pulsating nature of this object.

The binarity of KIC 6951642 is not yet certain, although a combined (RV+TD) solution is partly feasible. The reason why some p modes show a similar long-term behaviour of their TDs while

others (such as the strongest p mode) do not, is an obstacle to this interpretation. However, it could be that some of the modes show intrinsic phase variability.

The next step would be to perform an evolutionary plus seismic modelling of this hybrid pulsator, which could become challenging due to the combined effects of significant rotation and probable stellar activity, as well as possible binarity.

Acknowledgements. ASG acknowledges support from the Max Planck Society grant 'Preparations for PLATO science'. The authors appreciate the discussions with Dr. Daniel Reese at LESIA, Observatoire de Paris. The authors thank the *Kepler* and TESS teams for their efforts to provide all the observational data and light curves to the public and the referee for constructive comments. The authors also thank the HERMES Consortium for enabling the production of the high-resolution ground-based spectra. This research made use of LightKurve, a Python package for *Kepler* and TESS data analysis (LightKurve Collaboration et al. 2018). This work is based on data from the European Space Agency (ESA) mission *Gaia* (<https://www.cosmos.esa.int/gaia>), processed by the *Gaia* Data Processing and Analysis Consortium (DPAC, <https://www.cosmos.esa.int/web/gaia/dpac/consortium>). Funding for the DPAC has been provided by national institutions, in particular the institutions participating in the *Gaia* Multilateral Agreement.

References

- Aerts, C., Christensen-Dalsgaard, J., & Kurtz, D. W. 2010, *Asteroseismology* Aizenman, M., Smeyers, P., & Weigert, A. 1977, *A&A*, 58, 41
 Antoci, V., Cunha, M., Houdek, G., et al. 2014, *ApJ*, 796, 118
 Antoci, V., Cunha, M. S., Bowman, D. M., et al. 2019, *MNRAS*, 490, 4040
 Bailer-Jones, C. A. L., Rybizki, J., Fouesneau, M., Mantelet, G., & Andrae, R. 2018, *AJ*, 156, 58
 Balona, L. A. 2014, *MNRAS*, 437, 1476
 Balona, L. A., Daszyńska-Daszkiewicz, J., & Pamyatnykh, A. A. 2015, *MNRAS*, 452, 3073
 Balona, L. A. & Dziembowski, W. A. 2011, *MNRAS*, 417, 591
 Batten, A. H. 1973, *Binary and multiple systems of stars*
 Blanco-Cuaresma, S. 2019, *MNRAS*, 486, 2075
 Blanco-Cuaresma, S., Soubiran, C., Heiter, U., & Jofré, P. 2014, *A&A*, 569, A111
 Bouabid, M.-P., Dupret, M.-A., Salmon, S., et al. 2013, *MNRAS*, 429, 2500
 Bowman, D. M. & Kurtz, D. W. 2018, *MNRAS*, 476, 3169
 Breger, M. 1990, *Delta Scuti Star Newsletter*, 2, 13
 Breger, M. 2000, in *Astronomical Society of the Pacific Conference Series*, Vol. 210, *Delta Scuti and Related Stars*, ed. M. Breger & M. Montgomery, 3
 Breger, M., Stich, J., Garrido, R., et al. 1993, *A&A*, 271, 482
 Chen, X. & Li, Y. 2018, *ApJ*, 866, 147
 Christensen-Dalsgaard, J. 2000, in *Astronomical Society of the Pacific Conference Series*, Vol. 210, *Delta Scuti and Related Stars*, ed. M. Breger & M. Montgomery, 187
 Cox, A. N. 2000, *Allen's astrophysical quantities*
 D'Antona, F., Caloi, V., Montalbán, J., Ventura, P., & Gratton, R. 2002, *A&A*, 395, 69
 Duchêne, G. & Kraus, A. 2013, *ARA&A*, 51, 269
 Dupret, M. A., Grigahcène, A., Garrido, R., et al. 2005, *MNRAS*, 360, 1143
 Dupret, M.-A., Grigahcène, A., Garrido, R., Gabriel, M., & Scuflaire, R. 2004, *A&A*, 414, L17
 Fox-Machado, L. & Pérez Pérez, E. 2017, in *Revista Mexicana de Astronomía y Astrofísica Conference Series*, Vol. 49, *Revista Mexicana de Astronomía y Astrofísica Conference Series*, 87–87
 Gaia Collaboration, Brown, A. G. A., Vallenari, A., et al. 2018a, *A&A*, 616, A1
 Gaia Collaboration, Brown, A. G. A., Vallenari, A., et al. 2021, *A&A*, 649, A1
 Gaia Collaboration, Katz, D., Antoja, T., et al. 2018b, *A&A*, 616, A11
 Gaia Collaboration, Prusti, T., de Bruijne, J. H. J., et al. 2016, *A&A*, 595, A1
 García, R. A., Mathur, S., Salabert, D., et al. 2010, *Science*, 329, 1032
 García Hernández, A., Suárez, J. C., Moya, A., et al. 2017, *MNRAS*, 471, L140
 Gautschi, A. & Saio, H. 1995, *ARA&A*, 33, 75
 Grigahcène, A., Antoci, V., Balona, L., et al. 2010, *ApJ*, 713, L192
 Guo, Z., Fuller, J., Shporer, A., et al. 2019, *ApJ*, 885, 46
 Guzik, J. A., Kaye, A. B., Bradley, P. A., Cox, A. N., & Neuforge, C. 2000, *ApJ*, 542, L57
 Halbwachs, J.-L., Pourbaix, D., Arenou, F., et al. 2022, arXiv e-prints, arXiv:2206.05726
 Hambleton, K. M., Kurtz, D. W., Prša, A., et al. 2013, *MNRAS*, 434, 925
 Handler, G. 2013, *Asteroseismology*, ed. T. D. Oswalt & M. A. Barstow, Vol. 4, 207

- Kaye, A. B., Handler, G., Krisciunas, K., Poretti, E., & Zerbi, F. M. 1999, *PASP*, 111, 840
- Keen, M. A., Bedding, T. R., Murphy, S. J., et al. 2015, *MNRAS*, 454, 1792
- Lampens, P. 2021, *Galaxies*, 9, 28
- Lampens, P., Frémat, Y., Vermeulen, L., et al. 2018, *A&A*, 610, A17
- Lee, J. W. 2016, *ApJ*, 833, 170
- Li, G., Guo, Z., Fuller, J., et al. 2020, *MNRAS*, 497, 4363
- Lightkurve Collaboration, Cardoso, J. V. d. M., Hedges, C., et al. 2018, *Lightkurve: Kepler and TESS time series analysis in Python*, *Astrophysics Source Code Library*
- Lindegren, L., Klioner, S. A., Hernández, J., et al. 2021, *A&A*, 649, A2
- Lomb, N. R. 1976, *Ap&SS*, 39, 447
- Mathur, S., Salabert, D., García, R. A., & Ceillier, T. 2014, *Journal of Space Weather and Space Climate*, 4, A15
- Moe, M. & Di Stefano, R. 2017, *ApJS*, 230, 15
- Murphy, S. J., Moe, M., Kurtz, D. W., et al. 2018, *MNRAS*, 474, 4322
- Raskin, G., van Winckel, H., Hensberge, H., et al. 2011, *A&A*, 526, A69
- Reese, D., Lignières, F., & Rieutord, M. 2008, *A&A*, 481, 449
- Ricker, G. R., Winn, J. N., Vanderspek, R., et al. 2014, in *Society of Photo-Optical Instrumentation Engineers (SPIE) Conference Series*, Vol. 9143, *Space Telescopes and Instrumentation 2014: Optical, Infrared, and Millimeter Wave*, ed. J. Oschmann, Jacobus M., M. Clampin, G. G. Fazio, & H. A. MacEwen, 914320
- Ricker, G. R., Winn, J. N., Vanderspek, R., et al. 2015, *Journal of Astronomical Telescopes, Instruments, and Systems*, 1, 014003
- Saio, H. 1981, *ApJ*, 244, 299
- Samadi-Ghadim, A., Lampens, P., & Jassur, D. 2018a, *Acta Astron.*, 68, 425
- Samadi-Ghadim, A., Lampens, P., & Jassur, D. 2018b, *MNRAS*, 474, 5549
- Samadi-Ghadim, A., Lampens, P., Jassur, D. M., & Jofré, P. 2020, *A&A*, 638, A57
- Scargle, J. D. 1982, *ApJ*, 263, 835
- Schmid, V. S., Tkachenko, A., Aerts, C., et al. 2015, *A&A*, 584, A35
- Sekaran, S., Tkachenko, A., Abdul-Masih, M., et al. 2020, *A&A*, 643, A162
- Sekaran, S., Tkachenko, A., Johnston, C., & Aerts, C. 2021, *A&A*, 648, A91
- Southworth, J. 2021, *The Observatory*, 141, 282
- Uytterhoeven, K., Moya, A., Grigahcène, A., et al. 2011, *A&A*, 534, A125
- Van Reeth, T., Mombarg, J. S. G., Mathis, S., et al. 2018, *A&A*, 618, A24
- Xiong, D. R., Deng, L., Zhang, C., & Wang, K. 2016, *MNRAS*, 457, 3163
- Zhang, X., Chen, X., Zhang, H., Fu, J., & Li, Y. 2020, *ApJ*, 895, 124
- Zhang, X. B., Fu, J. N., Luo, C. Q., Ren, A. B., & Yan, Z. Z. 2018, *ApJ*, 865, 115

Table A1. Journal of the HERMES spectra of KIC 6951642.

BJD	Exp	S/N	RV	e_RV
2455820.493929	1800	78.14	-4.79	4.22
2455820.515356	1800	77.46	-5.13	4.68
2455823.517590	1500	62.50	-5.37	3.83
2455823.535549	1500	64.82	-4.89	4.13
2456515.563844	1000	47.08	-0.79	3.40
2456515.575998	1000	49.68	-1.59	3.19
2456601.325355	600	41.73	-1.40	4.04
2456605.334439	600	—	0.20	3.57
2456605.341963	600	—	-1.62	4.45
2457512.668146	1400	56.63	-3.24	3.19
2457514.527796	1700	56.23	-2.83	2.87
2457915.617435	1000	46.20	-10.86	4.64
2458679.501538	900	60.62	1.24	4.53
2458780.449374	1000	53.29	-0.01	3.42
2458787.333903	720	55.26	0.11	4.25
2458997.505925	1000	60.48	-0.43	3.19
2459091.424074	1000	51.57	-1.80	4.72
2459110.497660	1800	39.23	-1.99	2.49
2459391.482595	1000	45.77	-5.36	3.24
2459498.335626	1000	50.17	-8.16	3.50

Notes. Barycentric Julian dates (BJD), exposure times (Exp), signal-to-noise ratio's (S/N's), radial velocities (RV) and their corresponding uncertainties (e_RV).

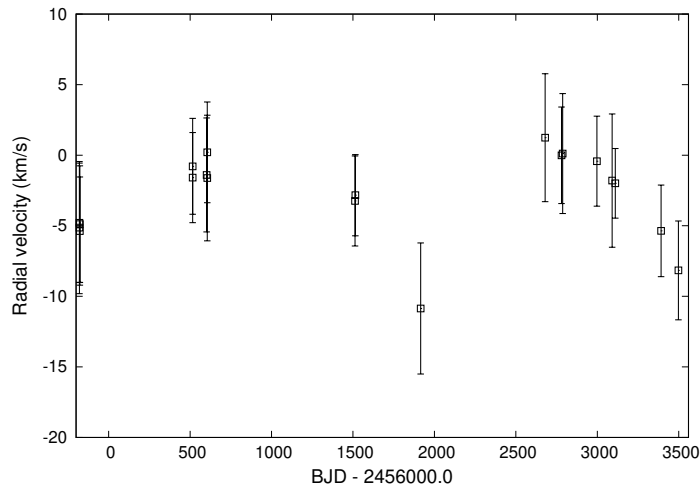

Fig. A1. RVs from the HERMES spectra of KIC 6951642 acquired over several years.

Table A2. Most dominant frequencies in low-frequency region (Fig. 7).

f_i	f (d^{-1}) ¹	A (mmag) ²	S/N	comb. ³	remark
f_1	2.2380	1.3910	59	f_{parent}	RS
f_2	2.9570	1.3764	77	f_{parent}	RS
f_3	0.7210	1.0962	31	f_{rot}	
f_4	0.7290	0.8743	27	$f_{\text{rot}} + f_{\text{ach1}}$	RS
f_5	1.4351	0.8659	30	f_{parent}	RS
f_6	0.7249	0.8654	27		
f_7	2.9559	0.7815	52	$f_{\text{ach1}} + 2f_5$	
f_8	1.5932	0.7688	29	f_{parent}	RS
f_9	0.7215	0.7507	24		

Table A2. continued.

f_i	f (d ⁻¹)	A (mmag)	S/N	comb.	remark
f_{10}	0.7258	0.6184	21		
f_{11}	2.9576	0.5642	40		
f_{12}	2.2360	0.5413	28	$f_2 - f_{\text{rot}}$	
f_{13}	1.4506	0.5148	22	$f_{\text{ach1}} + 2f_{\text{rot}}$	RS
f_{14}	1.5857	0.5029	21		
f_{15}	0.7224	0.4926	17		
f_{16}	0.7866	0.4557	17	f_{parent}	RS
f_{17}	1.5927	0.4550	21		
f_{18}	0.8020	0.4499	17	$f_1 - f_5$	
f_{19}	1.4436	0.4224	19	$f_{\text{ach1}} + f_5$	
f_{20}	2.2305	0.3730	22		
f_{21}	2.9546	0.3453	27		
f_{22}	2.9592	0.3433	28	$f_{\text{rot}} + f_1$	
f_{23}	0.7885	0.3418	13		
f_{24}	0.7175	0.3180	12		
f_{25}	0.2746	0.3091	12	$2f_{\text{ach1}} + 3f_{\text{ach2}}$	
f_{26}	1.4461	0.3072	15		
f_{27}	0.9956	0.2943	13	f_{parent}	RS
f_{28}	2.2388	0.2854	19		
f_{29}	3.6768	0.2847	32	$2f_2 - f_1$	
f_{30}	1.4498	0.2843	14	$f_{\text{ach1}} + 2f_{\text{rot}}$	
f_{32}	1.4581	0.2660	14	$2f_4$	
f_{33}	0.7156	0.2647	10		
f_{34}	1.4418	0.2562	13	$2f_{\text{rot}}$	
f_{35}	2.9539	0.2411	22		
f_{36}	0.4395	0.2327	10	$f_5 - f_{27}$	
f_{37}	1.4540	0.2235	12		
f_{38}	2.1673	0.2231	16		
f_{40}	2.0837	0.2111	14	$2f_5 - f_{16}$	
f_{42}	0.7913	0.2022	9		
f_{45}	0.2575	0.1939	8	$3f_{\text{ach2}}$	
f_{46}	0.7943	0.1896	8	$3f_{\text{rot}} + f_2$	
f_{47}	0.6183	0.1877	8		
f_{48}	3.2316	0.1815	21		
f_{50}	0.6023	0.1723	7		
f_{52}	1.4531	0.1707	10		
f_{53}	0.2378	0.1694	7		
f_{54}	1.5878	0.1693	10		
f_{55}	1.4359	0.1675	10		
f_{56}	1.3714	0.1675	10		
f_{57}	2.3951	0.1671	13		
f_{58}	0.5921	0.1662	7		
f_{60}	3.0202	0.1613	16	$f_5 + 2f_{\text{ach1}}$	
f_{62}	0.7196	0.1587	7	$f_2 - f_1$	
f_{63}	0.7847	0.1579	7	$f_{18} - 2f_{\text{ach1}}$	
f_{64}	1.3624	0.1508	9		
f_{66}	2.1658	0.1498	12		
f_{67}	0.7966	0.1487	7	$f_1 - 2f_{\text{rot}}$	
f_{68}	3.0239	0.1382	14	$f_1 + f_{16}$	
f_{69}	0.7986	0.1359	7		
f_{70}	1.4300	0.1346	8		
f_{71}	0.6503	0.1345	6		
f_{72}	3.7452	0.1333	19		
f_{73}	0.4637	0.1330	6	$f_{\text{rot}} - f_{\text{ach2}}$	
f_{76}	2.2300	0.1276	10	$f_1 - f_{\text{ach1}}$	
f_{78}	0.5274	0.1240	6		
f_{80}	2.1607	0.1234	10		
f_{81}	1.5056	0.1220	8		
f_{82}	1.1604	0.1193	7		
f_{83}	0.6317	0.1183	6	$2f_5 - 2f_1$	

Table A2. continued.

f_i	f (d ⁻¹)	A (mmag)	S/N	comb.	remark
f_{84}	1.4386	0.1182	8	$2f_2 - 2f_1$	
f_{86}	0.5509	0.1163	6		
f_{87}	2.9522	0.1135	12		
f_{88}	0.9587	0.1105	6	$f_{16} + 2f_{\text{ach}2}$	
f_{89}	2.1527	0.1102	9	$f_1 - f_{\text{ach}2}$	
f_{91}	3.6786	0.1078	16	$f_{\text{rot}} + f_2$	
f_{92}	0.2017	0.1058	5		
f_{93}	1.5749	0.1055	7	$f_8 - 2f_{\text{ach}1}$	
f_{94}	0.9825	0.1048	6		
f_{95}	3.0227	0.1022	11		
f_{98}	0.9668	0.1007	6	$f_2 - 2f_{27}$	
f_{99}	1.4473	0.1004	7		
f_{100}	0.5602	0.1003	5		
f_{102}	0.9936	0.0992	6		
f_{103}	0.4217	0.0985	5		
f_{105}	2.9506	0.0982	11		
f_{109}	2.2326	0.0953	8		
f_{111}	0.1945	0.0935	5		
f_{112}	0.5902	0.0932	5	$3f_3 - 2f_{16}$	
f_{113}	1.5802	0.0902	7		
f_{116}	0.7809	0.0889	5		
f_{118}	2.9630	0.0872	10		
f_{121}	2.1723	0.0848	8	$3f_{\text{rot}} + f_{\text{ach}1}$	
f_{122}	0.2831	0.0841	5	$3f_{\text{ach}1} + 3f_{\text{ach}2}$	
f_{124}	1.5849	0.0832	6	$f_8 - f_{\text{ach}1}$	
f_{125}	3.2129	0.0832	11		
f_{128}	1.5737	0.0810	6		
f_{129}	1.6460	0.0808	7	$f_2 + 3f_{\text{ach}2}$	

¹ The Uncertainties in frequency are $\epsilon_f = (0.04 - 3) \times 10^{-4}$ d⁻¹.

² The Uncertainties in amplitude are $\epsilon_A = (3 - 16) \times 10^{-3}$ mmag.

³ Col. 'comb.' lists the combinations. For the colours in Col. 'comb.' see table 6 and Sect. 5. RS: rotationally split g modes (Table 7 and Fig. 7.)

Table A3. Significant high frequencies ($f > 5. \text{d}^{-1}$) with the amplitudes and S/N larger than the associated mean values ($A > 0.0193 \text{ mmag}$ and $S/N > 7.7$) among all high frequencies.

f_i	$f \text{ (d}^{-1}\text{)}$	A (mmag)	S/N	comb.	remark
f_{31}	13.9651	0.2718	54		$f_{p_{\max}}$; RS; TDir
f_{39}	13.0064	0.2219	53		f_{parent} ; RS; TDr
f_{43}	14.3778	0.2018	43		f_{parent} ; RS; TDir
f_{44}	15.9634	0.1948	53		f_{parent} ; RS; TDir
f_{59}	14.9697	0.1652	39		f_{parent} ; RS; TDir
f_{85}	10.3107	0.1177	32	$3f_{260}-2f_{213}$	TDr
f_{104}	15.9627	0.0985	30		f_{parent} ; RS
f_{107}	15.4706	0.0976	28		f_{parent} ; RS; TDr
f_{119}	13.4902	0.0872	23	$3f_{\text{ach}2}+f_{260}$	f_{parent}
f_{123}	14.8528	0.0841	23		f_{parent} ; RS; TDr
f_{126}	12.7318	0.0823	24		f_{parent} ; TDr
f_{135}	16.4458	0.0766	27		f_{parent} ; RS
f_{143}	14.9677	0.0716	21		f_{parent}
f_{146}	12.5150	0.0708	22		f_{parent} ; RS; TDr
f_{154}	14.4500	0.0689	20		f_{parent} ; RS
f_{171}	14.1831	0.0627	18		f_{parent}
f_{178}	13.7274	0.0606	18		RS; TDr
f_{210}	11.3772	0.0497	18		f_{parent} ; RS
f_{212}	15.9654	0.0489	19		f_{parent}
f_{213}	14.6942	0.0485	16		f_{parent} ; RS
f_{218}	13.9660	0.0471	15		f_{parent} ; RS
f_{221}	8.3516	0.0453	17		
f_{223}	13.4492	0.0450	15		f_{parent} ; RS
f_{225}	10.1371	0.0442	14		
f_{226}	15.4231	0.0441	16		f_{parent} ; RS
f_{228}	14.8845	0.0438	15		f_{parent}
f_{230}	11.0008	0.0436	15		f_{parent} ; RS
f_{235}	7.8036	0.0420	16		
f_{242}	12.8819	0.0401	14		f_{parent}
f_{246}	13.3939	0.0391	13		f_{parent}
f_{259}	14.1668	0.0341	12		f_{parent} ; RS
f_{260}	13.2328	0.0341	12		f_{parent} ; RS
f_{264}	14.9410	0.0333	12		f_{parent}
f_{268}	14.9708	0.0319	12	$f_{\text{ach}2}+f_{228}$	f_{parent}
f_{269}	14.3688	0.0318	11		f_{parent}
f_{277}	15.4242	0.0298	12		f_{parent}
f_{288}	12.3408	0.0281	11		RS
f_{289}	14.4482	0.0275	10	$2f_{178}-f_{39}$	
f_{296}	14.2093	0.0266	10	$3f_{\text{ach}1}+f_{171}$	
f_{299}	12.9392	0.0264	10		
f_{302}	13.9538	0.0256	9	$f_{\text{rot}}+f_{260}$	
f_{303}	12.3687	0.0255	10	$2f_{259}-f_{212}$	
f_{304}	14.8516	0.0255	9		
f_{317}	13.9421	0.0231	9		
f_{320}	20.2742	0.0228	13		
f_{322}	10.4948	0.0223	8		
f_{326}	14.0506	0.0221	8	$f_{p_{\max}}+f_{\text{ach}2}$	
f_{327}	12.8864	0.0221	8		
f_{328}	10.8299	0.0218	8	$f_{230}-2f_{\text{ach}2}$	RS
f_{330}	14.4524	0.0214	8		
f_{331}	12.0166	0.0213	8	$3f_{218}-2f_{264}$	RS
f_{332}	13.9242	0.0211	8		
f_{337}	14.4585	0.0203	8	$f_{\text{ach}1}+f_{154}$	
f_{340}	13.5473	0.0199	8		
f_{341}	16.9162	0.0196	9		

Notes. For the colours in Col. 'comb.' see table 6 and Sect. 5. **RS:** Rotationally-split p modes (Table 8 & Fig. 9), **TDr:** frequency whose Time Delays show a similar long-term time delay trend (Fig. 3 & Sect. 2.2), **TDir:** frequency whose Time Delays show an incompatibility with general long-term time delay trend (Fig. 3 & Sect. 2.2). For the rest of the remarks see Table 6.

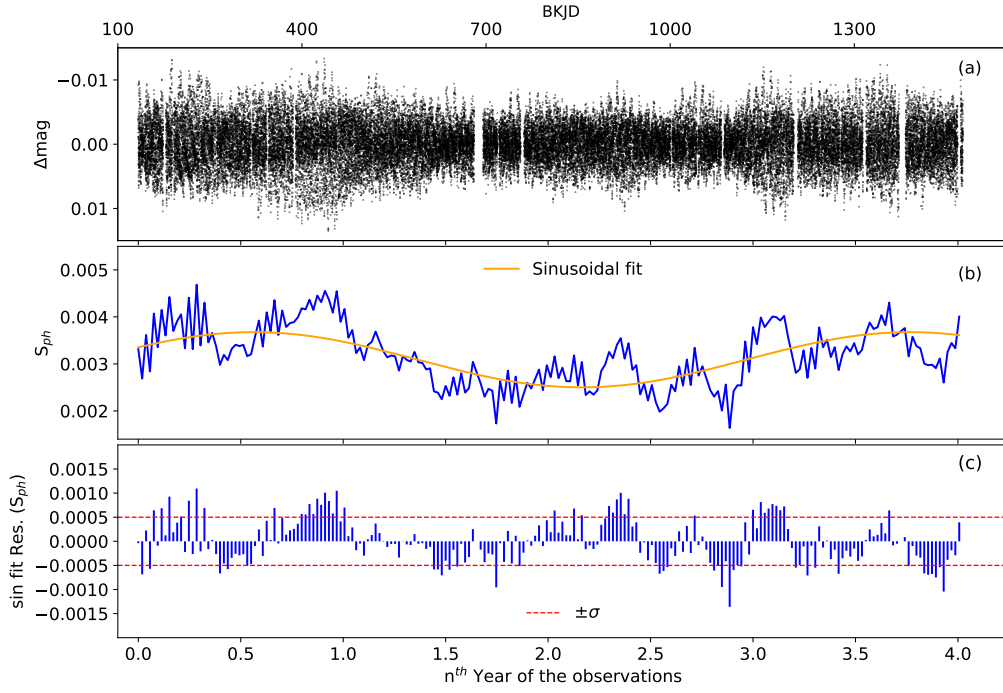


Fig. A2. The photospheric magnetic activity proxy S_{ph} of KIC 6951642. (a) *Kepler* LC light curve (1470.46 d) (b) Dispersion of the light curve on time scales of $5f_{rot}$ ($f_{rot} = 0.721 \text{ d}^{-1}$). Red dashed lines are an illustration of boundaries of maximum magnetic and minimum activity cycles of star. Orange curve presents the sinusoidal fit to S_{ph} in different cycles.

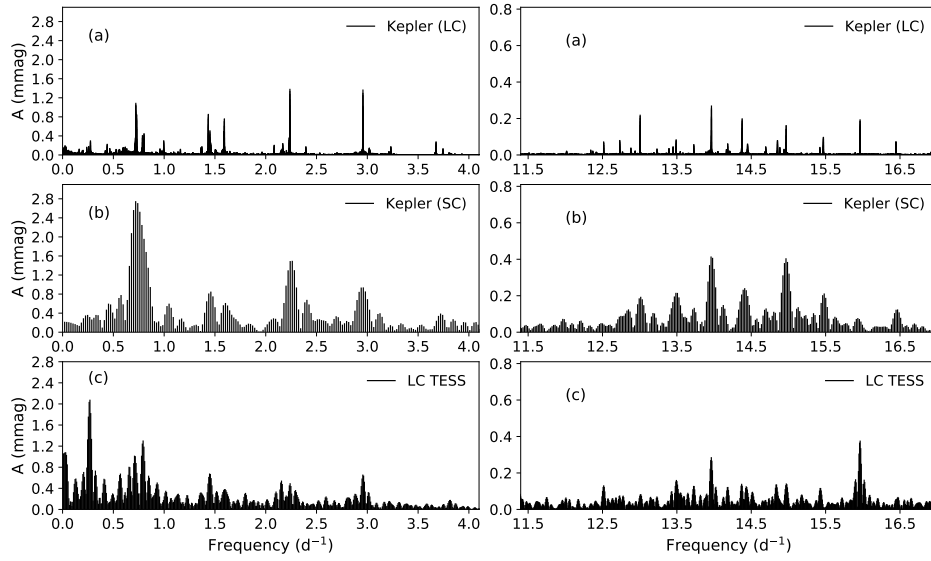


Fig. A3. A close-view to low- and high-frequency regions in Fourier Spectra KIC 6951642 from (a) *Kepler* Long Cadence (b) *Kepler* Short Cadence (c) TESS 1800 sec, sector 15. (Table 5).